Received: 11 September 2021 | Revised: 29 December 2021 | Accepted: 3 January 2022 | Accepted article online: 8 January 2022

DOI: 10.1002/pmic.202100224

Proteomics
Proteomics and Systems Biology

RESEARCH ARTICLE

Molecular histoproteomy by MALDI mass spectrometry imaging to uncover markers of the impact of *Nosema* on *Apis mellifera*

Camille Houdelet[1,2] | **Karim Arafah**[2] | **Michel Bocquet**[3] | **Philippe Bulet**[1,2]

[1] CR Université Grenoble Alpes, Institute for Advanced Biosciences, Inserm U1209, CNRS UMR 5309, Grenoble, France

[2] Saint Julien-en Genevois, Plateforme BioPark d'Archamps, France

[3] Apimedia, Pringy, Annecy, France

Correspondence
Philippe Bulet, Plateforme BioPark d'Archamps, 260 Avenue Marie Curie Arch-Parc 74166 Saint-Julien-en-Genevois, France.
Email: philippe.bulet@univ-grenoble-alpes.fr

Present address
Camille Houdelet, Adaptation et Adaptabilité des Animaux et des Systèmes (3AS), Station Expérimentale d'Aquaculture Ifremer, Chemin de Maguelone, 34250, Palavas-les-Flots, France

Camille Houdelet and Karim Arafah contributed equally to this work.

Funding information
France AgriMer, Grant/Award Number: 14-04R; H2020 Societal Challenges, Grant/Award Number: 773921

Abstract

Matrix-assisted laser desorption/ionization imaging mass spectrometry (MALDI IMS) is a powerful technology used to investigate the spatio-temporal distribution of a huge number of molecules throughout a body/tissue section. In this paper, we report the use of MALDI IMS to follow the molecular impact of an experimental infection of *Apis mellifera* with the microsporidia *Nosema ceranae*. We performed representative molecular mass fingerprints of selected tissues obtained by dissection. This was followed by MALDI IMS workflows optimization including specimen embedding and positioning as well as washing and matrix application. We recorded the local distribution of peptides/proteins within different tissues from experimentally infected versus non infected honeybees. As expected, a distinction in these molecular profiles between the two conditions was recorded from different anatomical sections of the gut tissue. More importantly, we observed differences in the molecular profiles in the brain, thoracic ganglia, hypopharyngeal glands, and hemolymph. We introduced MALDI IMS as an effective approach to monitor the impact of *N. ceranae* infection on *A. mellifera*. This opens perspectives for the discovery of molecular changes in peptides/proteins markers that could contribute to a better understanding of the impact of stressors and toxicity on different tissues of a bee in a single experiment.

KEYWORDS
Apis mellifera, imaging mass spectrometry, molecular histology, molecular mass fingerprints, *Nosema ceranae*

1 | INTRODUCTION

Over the past decades, thanks to technological improvements, matrix-assisted laser desorption/ionization imaging mass spectrometry (MALDI IMS) of tissues has gained popularity. MALDI IMS, historically developed by Caprioli and colleagues [1], is a label-free method that provides information on the spatial distribution of drugs and their metabolites [2], endogenous metabolites [3,4], biomarkers like lipids [5,6], glycolipids [7], and peptides/proteins [8–11], within sections of organs or whole-bodies/organisms [12–17]. In theory, this powerful tool can directly allow access, in a multiplex analysis, to hundreds or thousands of analytes in parallel on flash-freezing tissue sections [18] and on formalin fixed and paraffin embedded samples [19]. Due to these unique performances and its enhanced credibility, MALDI IMS has the power to facilitate mechanistic studies and discovery of potential molecular signatures of diseases for a deeper understanding of

the pathologically related processes. To date, MALDI IMS is commonly used in pharmaceutical research and industry to determine the importance of accumulation and metabolization of drugs in various tissues [2]. For example, MALDI IMS has been used to monitor the distribution of xenobiotic substances in skin [20,21] and artificial models of human epidermis [22]. Furthermore, MALDI IMS is also widely used in life sciences, biomedical, and pharmaceutical research and development on a multitude of biological matrices [23,24]. Advancements in MALDI IMS instrumentation for improved resolution and sensitivity, sample preparation workflows including innovative chemical strategies for on-tissue chemical derivatization or to generate novel matrices, and data management and processing, offer the ability to precisely quantify tissues molecular abundances with a high-resolution level [25–29]. MALDI IMS technology is now used for analyses of biological samples belonging to both plant (for reviews see [30–33]) and animal kingdoms including human specimens [23,34,35]. Given the increasing use of MALDI IMS on animal models, this approach was also investigated on different invertebrate models and for the first time in insects to map neuropeptides within the neuronal tissues of the cricket *Acheta domesticus* [36]. Subsequently, MALDI IMS was applied to bee models to follow the distribution of queen-signal compounds [37], analyze the neuropeptide distribution in the Africanized honeybee (*Apis mellifera*) brain [38,39] or to follow the degradation and toxicity of pesticides [40–42] and to identify the most abundant metabolites [43]. The European honeybee *A. mellifera* (Hymenoptera, Apidae) is the most managed pollinator in our agricultural systems and represents significant economic value [44,45]. The health of *A. mellifera* has been declining in many countries around the world, raising concerns about food resources [46,47]. Among a series of possible factors contributing to colony losses, infectious diseases caused by parasites and pathogens are significant contributors in altering bee health [48,49]. Among them, nosemosis is one of the possible factors that negatively impacts the honeybee health and especially *A. mellifera* population worldwide [50,51]. The causative agents are unicellular microsporidian parasites, essentially *Nosema apis* and *N. ceranae* [52]. *Nosema* spores are ingested into the digestive tract of the host where they can develop and multiply intracellularly before being expelled in the fecal matter following destruction of epithelial cells [53]. *Nosema* disease affects colony performances and bee health by many processes [54]. The impact of *Nosema* disease at the individual level includes numerous physiological alterations, such as (i) metabolic changes [55,56], (ii) energy stress/management [56], (iii) pheromone and hormone production [57], (iv) inhibition of epithelial cells apoptosis [58], (v) immune function suppression [55,59,60], (vi) life span shortening [56,61,62], (vii) cognitive deficits [63,64], (viii) acceleration of transition to forager activities [65], and (ix) changes of gut microbiota [66]. We recently conducted study with the aim to decipher the impact of a per-os inoculation of *A. mellifera* with spores of *Nosema* on the first off-gel proteomics on the different anatomical sections of the gut [67]. Upon oral infection, we observed at an early stage of the infection (4 days) that midgut proteins were the most altered (50 down-regulated, 16 up-regulated) compared to the control experiment with most of them being involved in metabolic and oxidative phosphorylation pathways [67]. To pursue our investigations on the underlying molecular mechanisms, MALDI IMS was conducted on the entire body of *A. mellifera* in this context in order to follow and establish the first comprehensive spatial histo-proteomics picture of the impact of *Nosema* infection on whole bee sections. The aim of the present work was to propose an experimental workflow for the study of the impact of a stressor in bee tissues by MALDI IMS. Specifically, we combined two MALDI MS approaches, MALDI molecular mass fingerprints (MALDI MFP), and MALDI IMS to generate molecular tissue signatures (gut, thoracic muscles, brains, hypopharyngeal glands, and hemolymph) and histo-molecular images of honeybees challenged with spores of *Nosema*. By combining these two MALDI approaches, we highlighted that *Nosema* did not exclusively impact the gut tissue, which is in agreement with our findings related to the molecular consequences of *Nosema* infection on the immune response, on the thoracic muscles and on the nervous system.

Significance of the study

Among pollinating insects, bees play a critical role in boosting reproduction of wild and commercial plants and thus contribute to the preservation of plant biodiversity and sustainability of food webs. In the last few decades, domesticated and wild bees have been subjected to biotic and abiotic threats causing various health disorders. In our proposed manuscript, we focus on nosemosis, an infection caused by a single-cell microsporidian parasite *Nosema* being the causative agent, which chronically infects the digestive tract of honeybees. Therefore, developing solutions to improve bee health including nosemosis is increasingly necessary, but still lacking. Here, we focused our investigations on the development of MALDI molecular mass fingerprint (MALDI MFP) and its integration with MALDI imaging mass spectrometry (MALDI IMS) to monitor which tissues would be impacted in a comparison between *Nosema*-infected and non-infected Western honeybees *Apis mellifera*.

2 | MATERIALS AND METHODS

2.1 | Chemicals

Trifluoroacetic acid (TFA), Acetonitrile (ACN), Methanol (MetOH), Ethanol (EtOH), Chloroform were purchased from Carlo Erba (Val de Reuil, France). Water was from Merck (Merck Millipore, Billerica, MA), Sodium carboxymethyl cellulose polymers (90 and 250kDa), 2,5 Dihydroxybenzoic acid (DHB, purity >99% by HPLC), Sinapinic acid (SA, purity ≥99% by HPLC), α-Cyano-4-hydroxycinnamic acid (4-HCCA, purity ≥99% by HPLC), Hematoxylin solution (Gill No. 3, IVD quality),

and Phosphate buffer saline (PBS) were purchased from Sigma Aldrich (France).

2.2 | Biological materials

For the achievement of MALDI MFPs approach, Buckfast adult bees were collected in a field apiary at the Plateforme BioPark d'Archamps (Archamps, France), *Nosema* non-infection was confirmed by microscopical observation of gut content. Concerning the MALDI IMS approach a brood frame was collected in June 2020 from one colony of Buckfast bees in a field apiary at the Plateforme BioPark d'Archamps (Archamps, France). Emerging honeybees were placed in plastic cages (Ickowicz, France) and maintained in incubators at 33°C ± 1°C and 60% ±20% relative humidity. During the first day, the bees were fed with syrup (InvertBee, Alp'Abeilles, France) ad libitum. The detailed experimental workflow was described in our previous study [67]. Briefly, 24 h after emergence, the syrup was removed for 15 h. Then, honeybees were placed individually in a homemade box and fed with 10 μl of syrup supplied with *Nosema ceranae* spores (100,000 spores per bee). After consuming the solution, bees were placed in a new collective box according to the experimental condition (control and inoculated bees). Sixteen days after inoculation, five control, and three infected bees were collected and immediately subjected to the inclusion process. The infection was confirmed by microscopic observation of the gut contents of an inoculated bee.

2.3 | Sample preparation for MALDI MFPs

For the achievement of the MALDI molecular mass fingerprints (MFPs), thoracic muscles, brains, and hypopharyngeal glands were collected from six worker bees under a binocular. Brains and hypopharyngeal glands were dissected according to the procedure of Carreck and collaborators [68]. The collected tissues were rinsed in PBS and kept at -80°C until use. The digestive tract of 12 bees were individually dissected from 1-day-old bees and segmented in three sections: the crop, the midgut and ileum, and the rectum. Gut tissues were washed in PBS and then placed in low protein binding tubes (LoBind, Eppendorf, France) containing 20 μl of TFA 1% and vortexed. Hemolymph was collected from the same 12 bees according to the procedure published by Arafah and colleagues [69].

For MALDI MFP spectra acquisition, brain, hypopharyngeal glands, and muscles were supplemented with 10 μl of TFA 1%, crushed on a MALDI polished target plate (Bruker Daltonics, Germany) and covered by 1 μl of TFA 1%. Tissues were then covered with 1 μl of a 10 mg/ml 4-HCCA matrix solution prepared in 70% ACN with TFA 2.5% acidified water (v:v). Gut sections were vortexed and 1 μl of the suspension was laid on the MALDI polished target plate. After drying the droplet was covered with 1 μl of a 15 mg/ml 4-HCCA solution prepared as above. MALDI MFPs spectra were recorded with an AutoFlex III – Smartbeam MALDI MS as described below. At the end of mass spectra acquisition, an average spectra representative to each tissue was generated using the mMass software v5.5.0.

2.4 | Sample preparation for MALDI IMS

To obtain histological blocks for MALDI IMS, honeybees were anesthetized using carbon dioxide and individually embedded into a 2% (w:v) solution of low viscosity 90kDa carboxymethyl cellulose (CMC) polymer prepared in ultrapure water. Additionally, the embedded bees were instantaneously vented for 20 min under 600 mbar vacuum using a home-made device apparatus to ensure optimal bee bodies inclusion; the remaining air from the bees' respiratory system and from their cuticles vicinity was thereby substituted with low viscosity CMC. The prepared bodies were then transferred into a filled tube with a chilled solution of the 250kDa CMC polymer. Once prepared, the samples were stored at -80°C for 24 h before being sliced.

Figure 1 summarizes the overall experimental workflow designed to map peptides and proteins from the entire body of *A. mellifera* using MALDI IMS.

Regarding sample preparation dedicated to MALDI IMS, before being sliced, the CMC-embedded body blocks were transferred from -80°C inside a cryomicrotome (Leica CM1950, Germany) maintained at -20°C and left to reach this appropriate cutting temperature for 15 min. Series of fresh frozen cryosections (15 μm thickness) were performed and collected onto classical histological slides (Dominique Dutscher, France). Cryo-sections were stained for 20 s using hematoxylin. Serial sections were also collected and transferred onto conductive Indium Tin Oxide (ITO)-coated glass slides (Bruker Daltonics, Germany). Before processing, structural lipids present on the surface of the tissue sections were washed out by three baths in pure ethanol (only immersion followed by total drying of slice between each rinsing) and one bath in pure chloroform (a one-second immersion). The images of tissues were then digitized using the Nikon CoolScan 9000 (Nikon, Japan) for automated MALDI IMS process teaching and the Mirax high-resolution desktop microscope (Zeiss, Germany) for observations of histological features. The tissue sections were coated with a solution of DHB matrix by spraying with the ImagePrep nebulizer (Bruker Daltonics, Germany), using two runs of the method provided by the manufacturer (DHB_standard_1). Series of protocols summarized the matrix preparations, the tissue slices delipidation and the number of automated matrix deposition that were tested prior to consider the 20 mg/ml DHB matrix dissolved in MetOH/Water (50/50; v/v) acidified with 0.2% TFA final concentration as the matrix solution throughout this study (Table S1).

2.5 | MALDI parameters

MALDI MFPs (mass range 600–18,000 Da) and MALDI IMS (mass range 1000–18,000 Da) spectra were acquired in a positive ion linear mode using an AutoFlex III - Smartbeam MALDI mass spectrometer equipped with a 200 Hz 355-nm frequency-tripled Nd:YAG laser

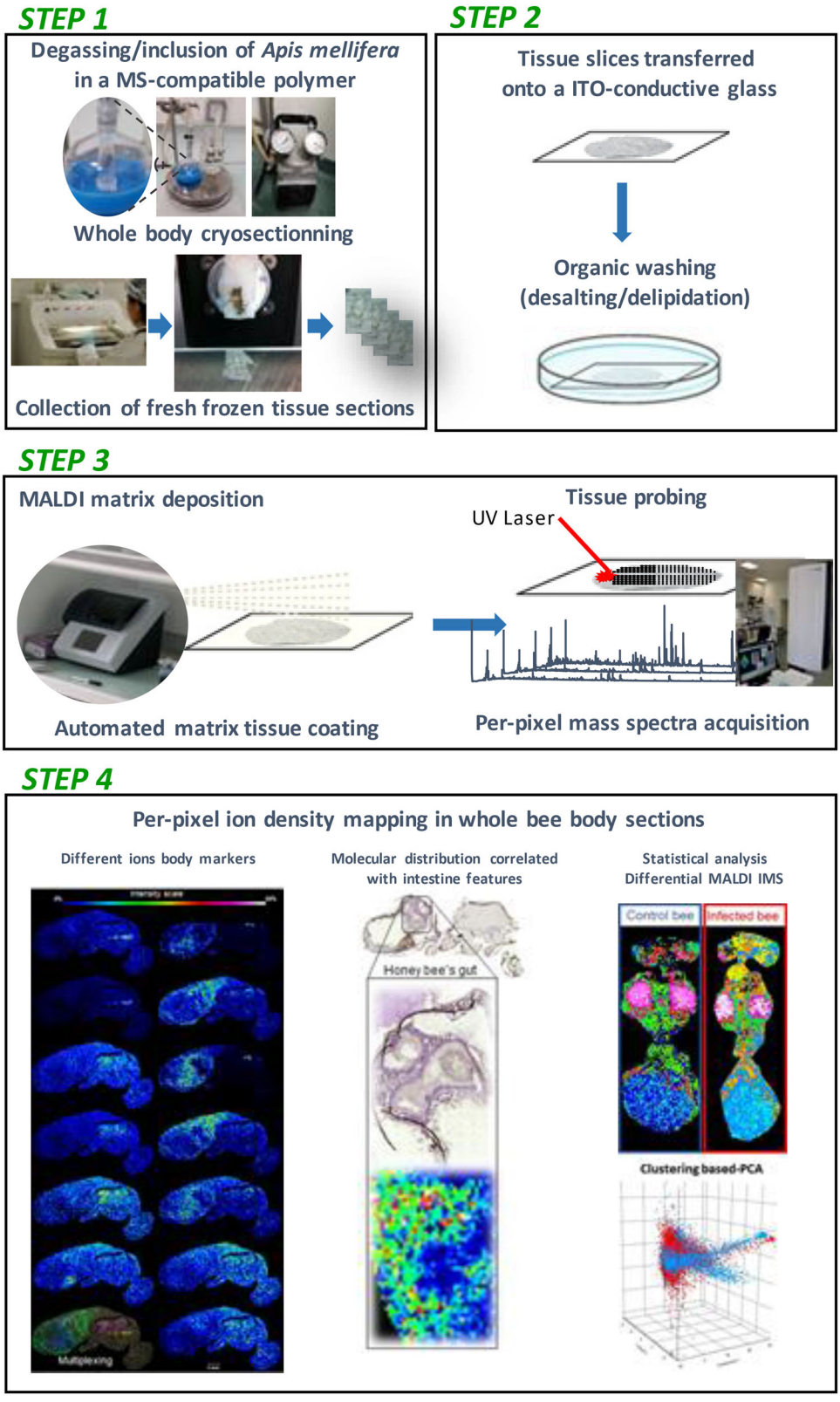

FIGURE 1 Whole-body MALDI IMS workflow applied to *Apis mellifera*. **Step 1**: Vacuum-degassing of the entire bee in a low viscosity 90 kDa carboxymethyl cellulose (CMC) polymer prior inclusion into a 250 kDa CMC polymer, freezing at -80°C and cryosectioning (15 μm thickness). **Step 2**: Whole bee body cuts transfer onto ITO-conductive glass slides (with subsequent organic baths for delipidation and desalting) and histological glass slides (histological features). **Step 3**: Matrix coating of the cuts on ITO slides using the automated piezoelectric nebulizer (ImagePrep, Bruker) and laser probing of the whole bee body tissue surface using MALDI MS (AutoFlex III Smartbeam, lateral resolution 60 μm). **Step 4**: Peptide and protein mapping with an application of differential MALDI IMS strategy to reveal specific markers correlating with nosemosis using FlexSeries and SCiLS software

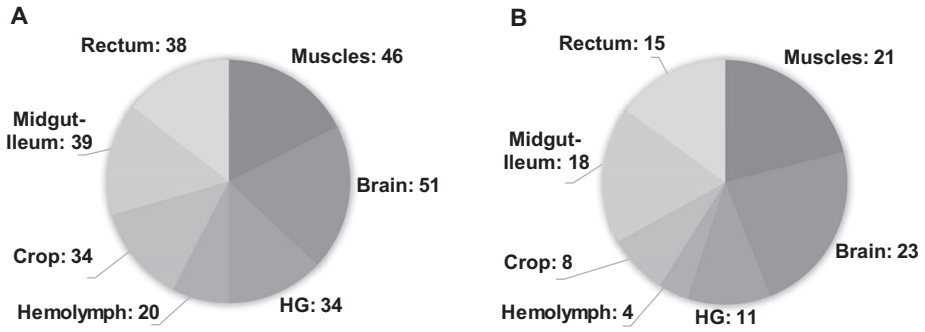

FIGURE 2 Number of potential markers identified in honeybee tissues. The list of peaks was first (A) extracted without comparison and then (B) the number of unique peaks presenting as potential markers of honeybee tissues. Abbreviation: HG, hypopharyngeal glands

(Bruker Daltonics, Germany) according to the analytical conditions and MALDI datasets post processing summarized in Table S2. The instrument was calibrated using a mixture of two sets of peptides (APISCAL) and proteins (ProtMix) covering the dynamic range of interest. The composition of the homemade APISCAL is the following: synthetic pure Apidaecin and Abaecin, two antimicrobial peptides from *Apis mellifera* (average *m/z* of 2109 and 3879, respectively), synthetic pure melittin, the major venom component, (average *m/z* of 2847); and ETD, a recombinant peptide, (average *m/z* of 4839). ProtMix (Protein Calibration Standard I, Bruker Daltonics) is a manufacturer-available mixture of four peptides and proteins (Insulin, Ubiquitin, Cytochrome C and Myoglobin at average *m/z* of 5734, 8565, 12,360, and 16,952, respectively).

3 | RESULTS AND DISCUSSION

3.1 | Tissue signatures by direct MALDI profiling experiment on honeybee organs

In this study, we identified potential features of six honeybee tissues (brain, hypopharyngeal glands, thoracic muscles, crop, midgut and ileum, and hemolymph) by generating their molecular mass fingerprints (MFPs) using MALDI mass spectrometry. This approach which has been greatly improved over the past 20 years, has demonstrated its feasibility, robustness and cost-effectiveness in identifying a wide range of microorganisms (e.g., bacteria, mycobacteria and certain fungal pathogens [70], parasites [71,72] and more recently some microsporidia pathogenic for honeybee [73]. We also used MALDI MFPs to monitor the impact of experimental microbial infections in honeybee hemolymph [69]. To create model MFPs, an average spectrum for each tissue was recorded as the most representative histo-molecular signature of the tissues (Figure S1). From these average spectra, a total of 46 molecular-related ions in muscles, 51 in brain, 34 in hypopharyngeal glands, 20 in hemolymph, 34 in crop, 39 in midgut and ileum and 38 in rectum were recorded between *m/z* 1000–14,000 (Figure 2A and Table 1). Finally, 21 molecular-related ions in muscles, 23 in brain, 11 in hypopharyngeal glands, 4 in hemolymph, 8 in crop, 18 in midgut and ileum, and 15 in rectum were found specific for each tissue between the mass range considered (Figure 2B and Table 1). The number of molecular-related ions was considerably reduced due to unavoidable cross contamination between some tissues and the hemolymph that infiltrates all tissues. Using MALDI MFPs, we obtained molecular mass signatures for the (i) brain, (ii) hypopharyngeal glands, (iii) thoracic muscles, (iv) hemolymph, and (iv) three anatomical sections of the gut tissue (crop, midgut-ileum and rectum) to serve their identification in situ by MALDI IMS.

3.2 | Experimental workflow for MALDI IMS on the honeybee model: from tissue embedding to MALDI imaging

The MALDI IMS method was introduced less than 25 years ago and revealed to be an effective technique to investigate the biological and physiological functions in bees. For instance, *Apis mellifera* brain neuropeptides were mapped in order to correlate the aggressiveness and ontogeny with the obtained neuropeptide signatures [38,39]. More recently, Zhang and colleagues used MALDI IMS to evaluate the degradation and the toxicity of two neonicotinoid pesticides in honeybees through oral and contact exposures [74]. Tissue processing describes the steps required to take an animal or human tissue from fixation to the state where it is completely infiltrated with a suitable histological wax to make it embedded ready for cryosection cutting on the microtome.

In our study, we implemented MALDI IMS protocol from honeybee preparation to whole-body scale imaging of the bee to investigate the molecular pattern changes in the context of nosemosis. The proposed workflow outlines the different steps involved in preparing a fully infiltrated and embedded honeybee, ready to be cryosectioned on a cryomicrotome on different cutting planes.

3.2.1 | Inclusion and embedding optimization

As insects are protected by a stiff primary exoskeleton (cuticle), sectioning the whole insect is quite challenging compared to slicing individual organs or mammalian tissues. The first step of our experimental workflow was to include and embed the entire honeybee body under vacuum. To address this challenge, we focused on two successive solutions (low density for inclusion, medium viscosity for embedding) of

TABLE 1 Lists of peaks identified as potential molecular markers of honeybee tissues

Muscles	Brain	HG[a]	Crop	MG-Ileum	Rectum	Hemolymph[b]
1079.41	1006.70	2085.76	1083.17	1102.02	1372.47	1164.14
1332.07	1469.13	2281.84	1294.92	1171.32	1388.51	2109.57
1573.57	1493.09	3417.78	1855.03	1238.48	1403.51	2130.90
1596.21	1520.40	3433.18	1893.92	1276.49	1456.03	2856.29
2079.48	1955.78	3449.38	2470.96	1529.17	2455.90	3479.82
2096.17	3183.64	4198.13	5559.57	1586.06	2626.02	5963.16
2357.00	3528.53	4560.78	5608.00	1676.02	2739.00	
2378.83	4279.63	5434.26	9598.78	1691.81	2944.09	
2395.84	4865.73	6669.66		1807.92	6127.28	
2419.04	5200.75	6794.65		1963.28	8444.60	
3033.49	5394.43	13585.62		2704.57	8927.04	
3074.59	6225.36	5520.76		2833.40	9750.65	
3202.60	6653.74			3667.14	9914.29	
3240.58	6784.05			3944.06	9969.93	
4740.12	6996.48			4760.52	10133.69	
5382.27	7335.62			4802.24		
5845.06	7543.65			4843.13		
6064.92	8186.92			4880.33		
6200.82	8316.22					
8191.61	8470.00					
8591.33	8548.37					
	10204.10					
	10399.03					

Abbreviations: HG, Hypopharyngeal glands; MG, Midgut.
All values are expressed in *m/z*. Peaks used as tissue markers for the MALDI imaging are underlined in gray.
[a]For the hypopharyngeal glands, the molecular mass in red at 5520.76 is corresponding to Royalisin.
[b]For the hemolymph, the molecular masses in red at 2109.57 and 5963.16 are corresponding to the systemic immune peptides Apidaecin and to the Apis mellifera Chymotrypsin inhibitor (AMCI), respectively.

a MALDI IMS compatible polymer, namely carboxymethyl cellulose (CMC; Figure S2). This two-step approach is critical to remove the air entrapped in all externally contacting anatomical structures including the tracheal sacs beneath the hard cuticle and to preserve the anatomical structures during cryoslicing. To our knowledge, this is the first report on the use of a low viscosity CMC polymer solution to include and preserve histology in fresh frozen insect tissue sections. In their study, Pratavieira and colleagues seem not to embed the head but to apply an instantaneous head freezing step in nitrogen as described by Seeley and Caprioli [35,38,39] for mammals organs.

Following the inclusion, a 250kDa CMC polymer solution was preferred to the 90kDa polymer because of its higher viscosity as an embedding medium making thus a harder specimen block to slice. As reported in the literature, this type of embedding solution was previously recommended for tissue preparation for MALDI IMS analyses [75–77].

In their study, Zhang and collaborators mapped pesticides throughout the whole honeybees' body cryosections using the OCT (Optimal Cutting Temperature) polymer as embedding medium [74]. However, in other works, this embedding polymer was considered as non-suitable for MALDI imaging of small molecules (below 1kDa) as it easily protonates and therefore contaminates MALDI mass spectra [78,79] and favors subsequent potential ion suppression [80,81]. To circumvent this drawback, Truong and colleagues eliminated the OCT polymer from the tissue surface using an ammonium buffer to perform MALDI imaging lipidomics [82].

3.2.2 | Organ visualization using sagittal and frontal section axes

Visualizing the distribution of compounds (e.g., metabolites, lipids, peptides/proteins) among different organs of a honeybee may assist in responding to the impact of a stressor and in determining potential "molecular signatures" for specific organs. To obtain an exhaustive image of the impact of a stressor on *A. mellifera*, once included, the CMC embedded body blocks were cryosliced according to sagittal and frontal planes to image as many organs as possible that may be direct or indirect targets of the stressor(s) (e.g., infectious, pesticide). We initiated MALDI images of *A. mellifera* in a sagittal plane (e.g.,

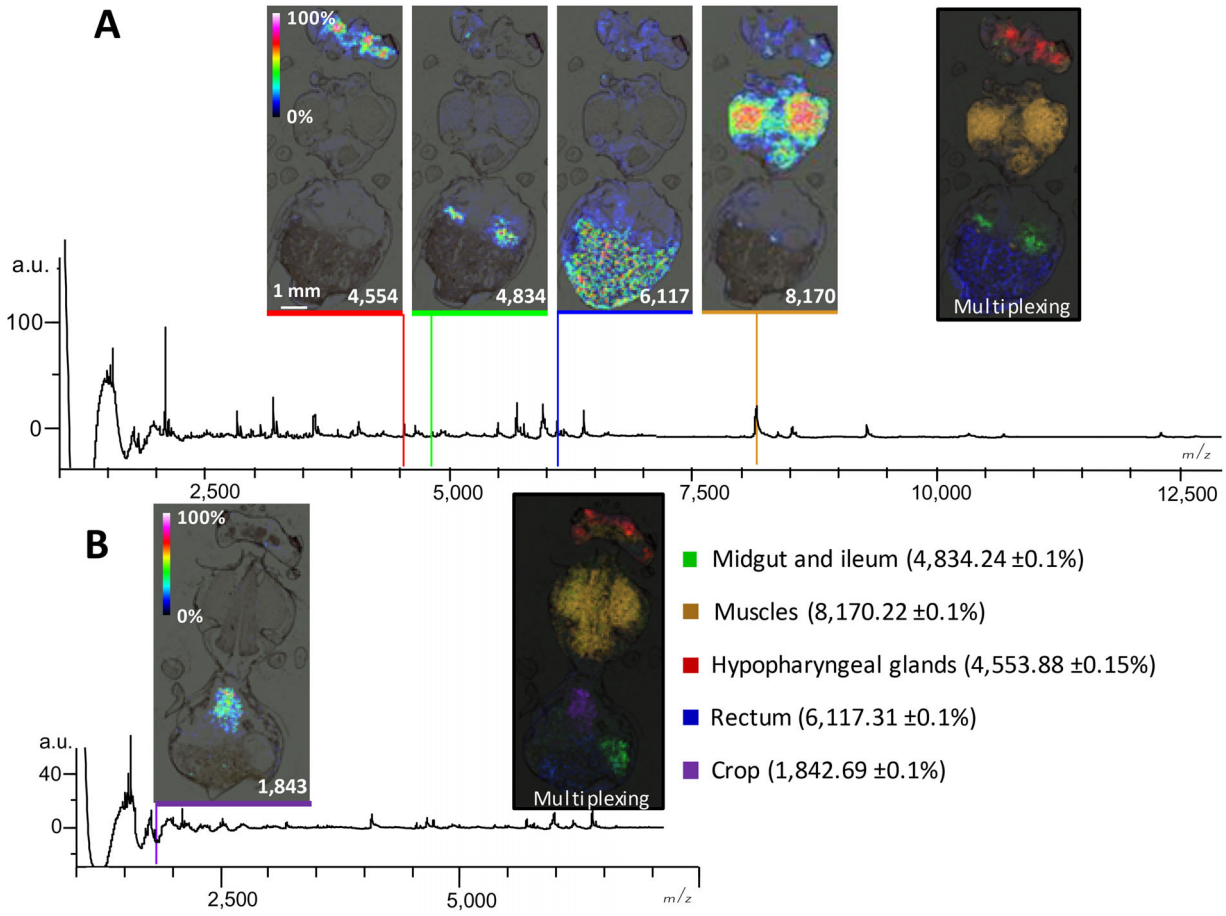

FIGURE 3 Molecular mass spectra and images of markers identified by MFPs extracted from MALDI IMS analyses of frontal whole-body sections of *Apis mellifera*. The potential markers of the hypopharyngeal glands (red), rectum (blue), muscles (orange), the midgut and ileum (green) were found in the general mass spectra on a first bee section (A) and the crop (purple) on a second bee section (B). Bar scale: 1mm. All values on pictures are expressed in *m/z*. Scale of intensity from 0% to 100% of the molecular-related ions

see Figure 1, Step 4 pictures on the left). Our results revealed that although we were able to get images of different body sections (head, thorax, and abdomen) details remained difficult to obtain. For example, we did not observe clear images of the central nervous system and more importantly of the different anatomical sections of the gut tissue, which may represent the main target of our infection model, nosemosis. To overcome this problem, sections in a frontal plane were prepared, this plane being often considered to be the most suitable for studying the abdominal content and especially the midgut as this proximal part of the bee gut tract twists around the midgut, the Malpighian tubules, and the ileum [68].

3.2.3 | Pretreatment of the tissue sections and matrix selection

Consecutively to inclusion, embedding and slicing, we first tested a combination of solvents to delipidate and desalt the tissue sections, a depletion step deemed important to optimize peptide/protein detection [80,83]. In a second step, we evaluated the quality of recorded spectral signal from direct tissue imaging using SA, 4-HCCA, DHB (Table S1), the three most frequently matrices employed. To assess tissue complexity, we looked at the ionic signal recorded from body segments (head, thorax, abdomen) through targeted tissue imaging of region of interest (ROI) *versus* whole body sections (Table S1). To achieve this, 15 μm of fresh frozen cryosections were prepared in sagittal and frontal planes, and ion peaks from the MALDI imaging spectra were extracted and compared. Their relative intensities were examined within the selected mass range of analysis (*m/z* 1000–20,000, Table S2) and with the lowest chemical background taken into account (data not shown). The best on-tissue imaging signal was obtained with DHB at 20 mg/ml prepared in a methanolic solution (Figure S3) following delipidation/desalting using a washing protocol based on three bathes in pure ethanol and one bath in pure chloroform (each bath 1 s). We tried various combinations of depletion and matrix, based on few studies existing on insects and specifically on bees. Pratavieira et al. (2014, 2018), selected a longer rinsed step and only with ethanol solutions and they applied a 4-HCCA matrix. At the beginning of our experiments, we also used the ethanol alone but we rapidly observed an improvement of spectra acquisition with addition of chloroform [38,39]. Concerning the matrix, they chose the HCCA, more appropriate for detection of small molecules, appropriate in their

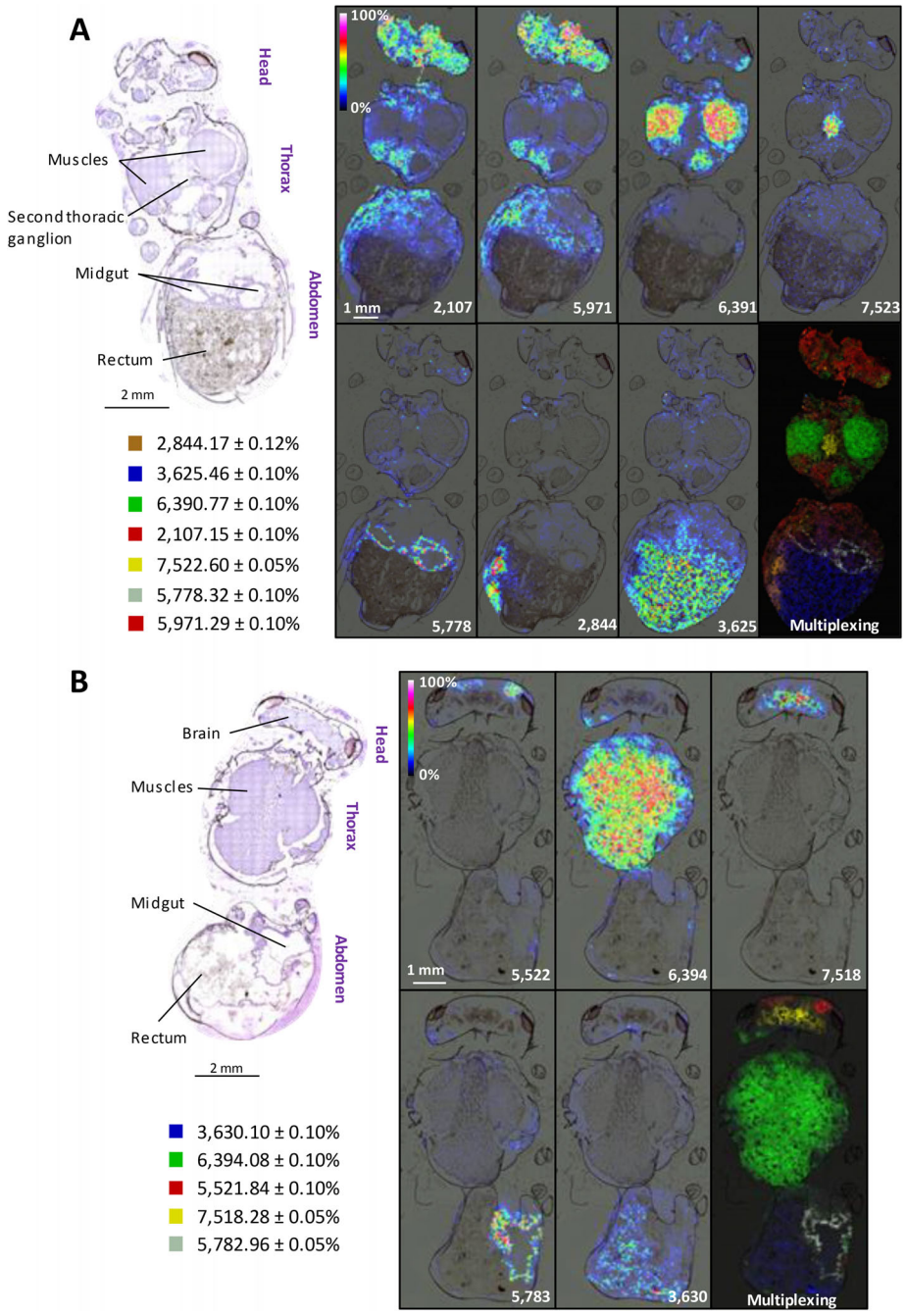

FIGURE 4 Molecular images of markers identifying bee tissues/organs. (A) Hematoxylin stained section of one honeybee cryosection showing the muscles, second thoracic ganglion, midgut and rectum, and MALDI images with tissue specific molecular-related ion markers. (B) Another honeybee stained cryosection showing the muscles, brain, midgut and rectum. The associated molecular images were observed and pictured in the specific tissues. All values on pictures are expressed in *m/z*. Scale of intensity from 0% to 100% of the molecular-related ions

case because they worked in the masse range 700–4000 Da. In our methodology, we proposed to recover sample with DHB to visualize ions in a larger mass range (mass range 1000–18,000 Da).

3.3 | Honeybee histo-molecular atlas

After optimizing the sample preparation for MALDI IMS using frontal cryosections of the honeybee, we compared the lists of the molecular-related ions identified in each bee tissues MFP with those imaged in the whole bee body. Considering a potential difference of 10 Da between the molecular-related ions recorded after MALDI MFP and those observed by MALDI IMS, one molecular-related ion marker was found representative for five (Table 1, highlighted masses in grey) of the seven tissues targeted in this study. In the molecular image (Figure 3A), we found four different molecular-related ion markers for the hypopharyngeal glands, the midgut combined to the ileum, the rectum, and the thoracic muscles including a *m/z* at 4554, 4834,

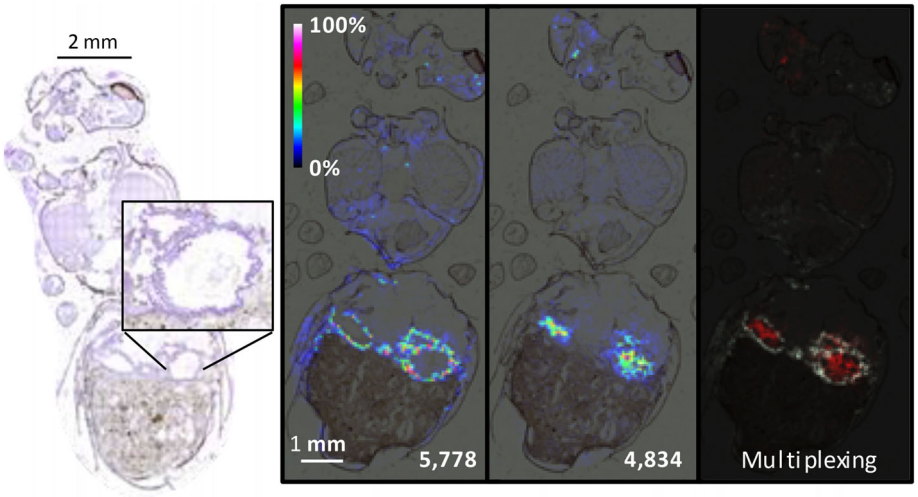

FIGURE 5 Molecular images of two markers of the midgut. The two markers of the midgut previously identified were observed and demonstrated a complementarity with the histological features between the midgut epithelium (*m/z* 5778) and the midgut content (*m/z* 4834). Intensity scale from 0% to 100% of the molecular-related ions

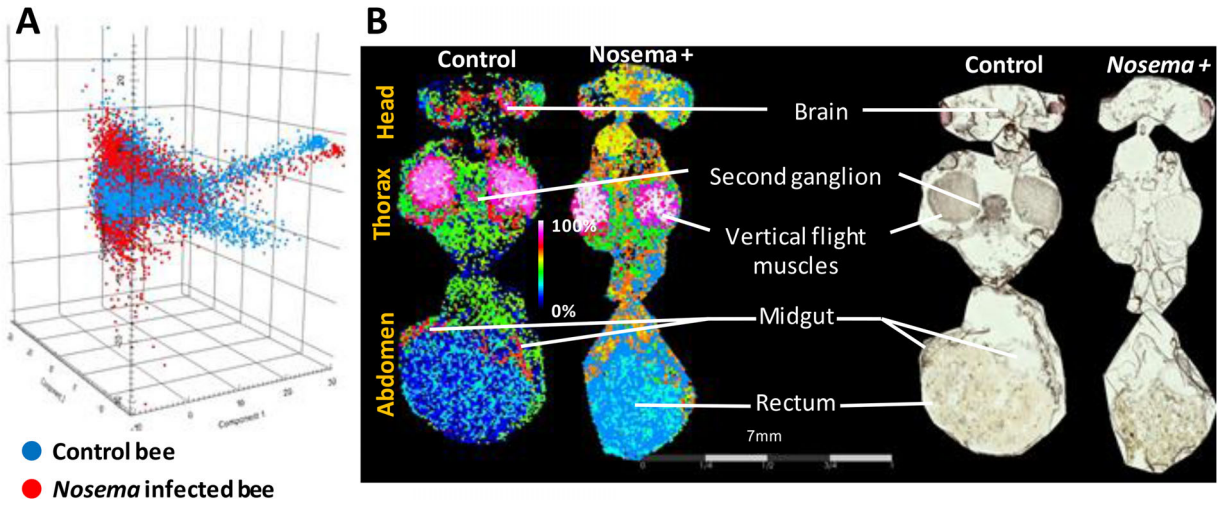

FIGURE 6 Principal component analysis (PCA) and spatial segmentation of whole-body imaging spectra from *Apis mellifera*. The spectra were submitted to unsupervised PCA (A), which discriminated the *Nosema*-infected honeybee from the control bee. The PCA-based molecular segmentation (B) evidenced specific clusters of spectra signatures through color patterns that match with histological features (right body pictures)

6117, and 8170, respectively. An additional molecular-related ion at *m/z* 1842 was found as a signature of the crop in a MALDI image generated from another bee (Figure 3B). The crop is not consistently visible since it depends on whether the bee has just eaten (crop larger than the rectum) or not (rectum larger than the crop). For example, the rectum mostly represented the total abdomen content, while we cannot recognize the crop. Considering the hemolymph peak list, among the molecular-related ions identified, the one corresponding to the immune peptide Apidaecin (2108.57 Da), and the *Apis mellifera* chymotrypsin inhibitor (AMCI, UniProtKB entry P56682, [84]; 5962.16 Da) were also recorded (Table 1, masses in red).

First, we imaged the hemolymph through Apidaecin (theoretical average *m/z* 2109.44) and AMCI (theoretical *m/z* 5963.81). A molecular-related ion at 2107.15 (Figure 4A) is close to the theoretical average value of Apidaecin and a second one at *m/z* 5971.29 is expecting to correspond to AMCI, a serine-type endopeptidase inhibitor we have structurally characterized (unpublished work, Plateforme BioPark d'Archamps, October 2020) and known to be circulating in the hemolymph [84]. In a second step, complementary molecular-related ions specific to the second thoracic ganglion (*m/z* 7523 Figure 4A) and to the brain (*m/z* 7518 Figure 4B), muscles (*m/z* 6391 Figure 4A; *m/z* 6394 Figure 4B), midgut (*m/z* 5778 Figure 4A; *m/z* 5782 Figure 4B) harboring villosities, and rectum content (*m/z* 3625 Figure 4A; *m/z* 3630 Figure 4B) were evidenced. Interestingly, additional tissues were imaged through specific ions. In the abdomen, the venom gland was at least depicted through the molecular-related ion of Melittin

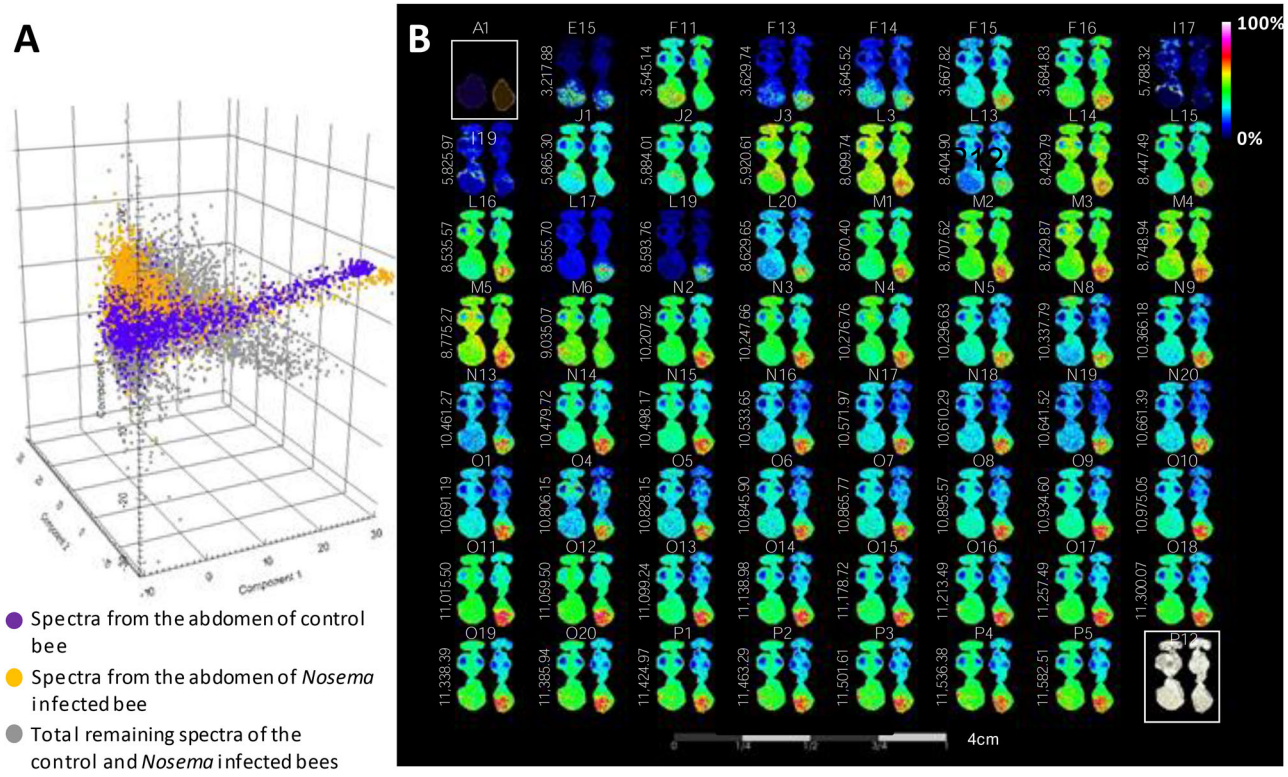

FIGURE 7 Discriminant PCA and differential ions patterns in abdomen from control *versus* infected honeybee by *Nosema ceranae*. The PCA analysis made with spectra from *Nosema*-infected *versus* control abdomen harbored different molecular patterns (A) and ions specifically expressed in either the nosemosis (right body) or in the control condition (left body) (B). Each depicted molecular-related ion (*m/z*) is detailed in the Table S4 and identifiable through its coordinates. The P12 coordinate corresponds to the histological view. The bee images in the left side are corresponding to a control, while the right-side images are from a *Nosema*-infected bee). Intensity scale from 0% to 100% of the molecular-related ions

at *m/z* 2844 (Figure 4A), the major component of bee venom [85,86]. Within the abdomen, the two molecular-related ions at *m/z* 5778 (Figure 4A) and 5783 (Figure 4B) imaged specifically the midgut epithelium.

The combination of MALDI MFP and MALDI IMS used in this study allowed us to discriminate the midgut epithelium from the gut content (Figure 5). These results show the robustness of our MALDI IMS workflow to prevent molecular-related ion delocalization within tissues, and prompt us to apply our workflow to follow the direct impact of nosemosis on the gut tissue, the vertical flight muscles, the nervous system and the hemolymph.

3.4 | Differential histo-proteomics changes in *Apis mellifera* following infection with *Nosema ceranae*

As part of this study, we experimentally infected honeybees with spores of *N. ceranae* and evaluated the consequences of this infection at the peptidomics/proteomics levels and for all body parts 16 days after inoculation. Nosemosis is a globally prevalent disease in domestic honeybees and its effects are diverse, impacting the honeybee from the cellular to the behavioral level [54]. We hypothesized the existence of an alteration of the peptidomics/proteomics profiles of the gut but also of other organs. We first focused our analyses on the primary target of spores for development, the gut [53]. Principal component analysis (PCA) based on MALDI IMS spectra from control versus infected bees with *N. ceranae* revealed discriminative molecular patterns along with the three first components (Figure 6A). To correlate these patterns with specific tissue locations, spectra were clustered and mapped using segmentation and each cluster is assigned a color and a specific molecular distribution throughout the bee body. As a result, clusters of spectra were specifically found in the brain and the second thoracic ganglion, in the vertical flight muscle and in the midgut (Figure 6B). The total detected ions are listed in the Table S3 and mapped in the Figure S4.

We refined our analysis by extracting spectra from the abdomen of the control and *Nosema*-infected bees. Based on these spectra, the PCA revealed discriminative profiles (Figure 7A) and 62 differentially expressed molecular-related ions could be retrieved from the analysis (Figure 7B, Table S3). First observations confirming the results obtained with unsupervised hierarchical clustering, the distribution of the 62 molecular-related ions mapped two patterns in the abdomen, namely the midgut and the rectum. The molecular-related ions at *m/z* 5788.32, 5825.97, 5884.01, and 5920.61 were found to be more intense in the midgut of the control bee compared to the infected one (Figure 7B, Table S3) whereas all the other molecular-related ions were distributed within the rectum and found to be more intense in the

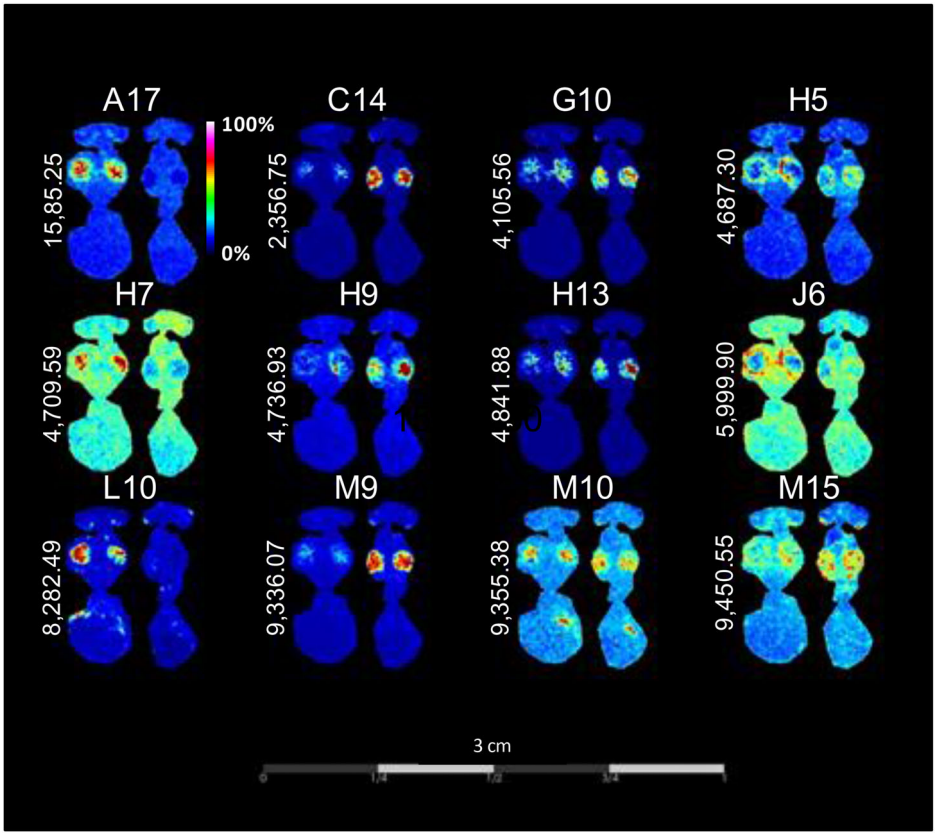

FIGURE 8 Tile view of twelve differentially expressed molecular ions in the bees' thorax following infection with *Nosema ceranae*. The mapped molecular-related ions (*m/z*) were differentially displayed between the control condition (left body) and the *Nosema*-infected bee (right body). These molecular-related ions are detailed in the Table S4 and identifiable through their coordinates (e.g., A17, C14, G10, and H5). Intensity scale from 0% to 100% of the molecular-related ions

infected bees. *N. ceranae* spores are known to destroy epithelial cells of the midgut when multiplying; this phenomenon could explain why some proteins were less intense in infected bees. As for the rectum, we could hypothesize that we observed some peptides/proteins of mature spores after being expulsed from the midgut. To identify those potential markers of spores, complementary experiments will be necessary. Alteration of the gut microbiota by the infection could also explain a change in the proteomic profile of the gut [87].

Studying the molecular impact of nosemosis in the honeybee also implies looking beyond the local response in the abdomen. As demonstrated in this study, MALDI IMS allowed the recording of hundreds of ions throughout the honeybee body regardless of the unsupervised *vs* supervised (Figure S4, Table S3) strategy used. Indeed, the pathology associated with *N. ceranae* infection is already described in literature [88] and different impacts were reported such as changes in metabolism [56] pheromone and hormone production [57], suppression of the immune function [55,59] or cognitive deficits [63]. All of these effects suggest an alteration of tissues involved in these deficient functions.

We used the efficacy of our MALDI IMS workflow to screen for all the differentially expressed signatures in the honeybee body and also noticed differential molecular patterns within the thorax (Figure 8, Table S4). Here again, three patterns of molecular distributions were observed. For the first one, molecular-related ions were found expressed in the vertical mass muscle with markers either over detected in the control (*m/z* 1585.25, 4709.59) or in the infected bee (*m/z* 2356.75, 4105.56, 4736.93, 4841.88, 9336.07, and 9450.55). Regarding the second pattern, molecular-related ions were also found in the vicinity of the vertical mass muscle and highly expressed in the control bee (*m/z* 4687.30 and 5999.90). Finally, the third pattern was represented by molecular ions depicted in the muscle and midgut epithelium only in the control condition (*m/z* 8282.49) or for the molecular-related ions at *m/z* 9355.38 in the muscle and the midgut content with equal distribution and intensity in both control and *Nosema* infection conditions. We hypothesize that the alteration of the muscles peptide/protein patterns could reflect the impact of *Nosema sp.* on flight abilities that are often observed in natural environment [89] as the result of energetic stress caused by this disease [56]. To have a better understanding of the molecular impact of nosemosis on the honeybee, we will develop additional tissue-targeted bottom-up proteomics following the work of Houdelet and collaborators [67].

In order to pinpoint infection-related tissue markers, we naturally had a look at the systemic response in the hemolymph as a mirror of molecular changes following infections. To visualize the hemolymph distribution, we crossed the MALDI IMS (Figure S4, Table S3) and MALDI MFP (Table 1) datasets and matched up the two

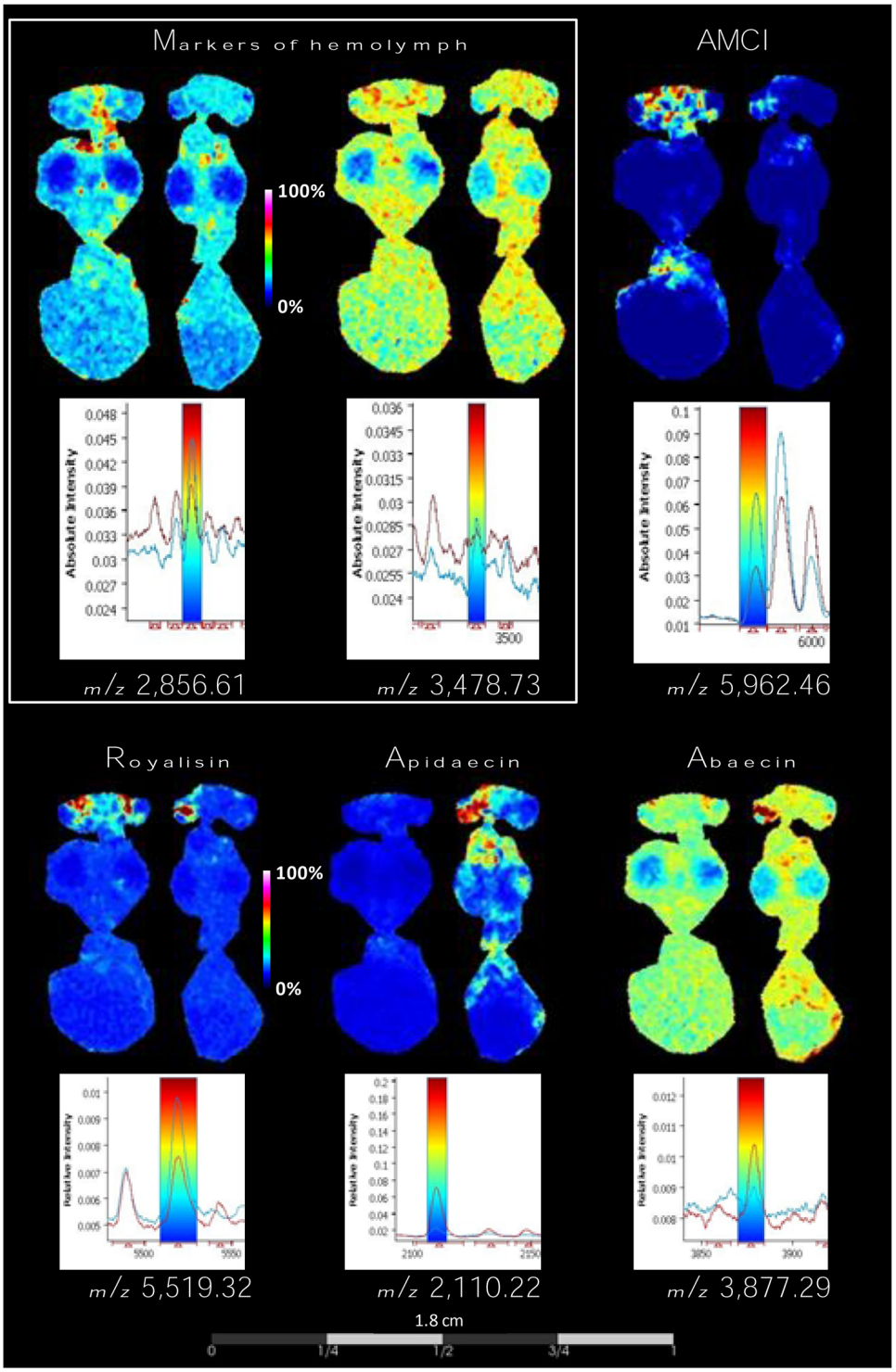

FIGURE 9 Differential abundance intensities and mapping of characteristic markers expressed in the hemolymph, the hypopharyngeal gland and the thoracic muscles with respect to the histology and physiology of the honeybee. Two molecular-related ions correlating with the hemolymph (*m/z* 2856.61 and 3478.73) were found as markers (*m/z* 2856.61 and 3478.73). The *Apis mellifera* chymotrypsin inhibitor (AMCI) was found mostly expressed in the hemolymph in the head and abdomen (*m/z* 5962.46) of the control experiment. The Royalisin (m/z 5519.32) was found depicted in the head, while Apidaecin (*m/z* 2110.22) and Abaecin (*m/z* 3877.29) were found correlated with hemolymph in the head, thorax, and abdomen. The bee images in the left side are corresponding to a control, while the right-side images are from a *Nosema*-infected bee. Intensity scale from 0% to 100% of the molecular-related ions

molecular-related ion *m/z* 2856.61 and 3478.73 (Figure 9), which are not described in scientific literature to the best of our knowledge. By this means, we could also assign the hemolymphatic distribution of the *Apis mellifera* chymotrypsin inhibitor (AMCI; theoretical molecular-related ions at *m/z* 5962.46), which was observed intensely in the head and proximal section of the abdomen from the control bee. Interestingly, the distribution of the serine-protease inhibitor AMCI in the infected honeybee did not show such a similar and intense pattern (Figure 9). The role of AMCI is still unclear but generally speaking, the serin protease type "chymotrypsin like" are implied in biological process like digestion, coagulation, or cellular and humoral immunity [90]. Regarding the systemic inducible immune response, the three antimicrobial peptides (AMPs), Royalisin also known as defensin-1 (*m/z* 5519.32), Apidaecin (*m/z* 2110.22), and Abaecin (*m/z* 3877.29) could be retrieved from our MALDI IMS datasets. Royalisin was only mapped in the heads of both control and *Nosema*-infected bees with no evidence of differential profiles. This molecule is also associated to the hypopharyngeal glands, found in the head of bees. Unlike Apidaecin, which is located throughout the infected bee and very slightly detected in the control bee, the hemolymphatic distribution of Abaecin was mainly in the head and between the midgut as well as the rectum, and was found more expressed in the infected bee. Many studies carried out on bees experimentally infected with *Nosema* spores have shown that the expression of the genes encoding AMPs was altered [55,59,91,92]. In their transcriptomic studies, Schwarz et Evans, also reported an increase expression of the *apidaecin* and *abaecin* genes seven days after inoculation of *N. ceranae* spores [93].

4 | CONCLUDING REMARKS

In the honeybee, multistressors increase the risk of mortality by acting in concert on multifarious physiological pathways, resulting in alterations of tissue function. Like in other animal models, mass spectrometry imaging approaches could be used to predict the impact of health stressors on the honeybee. The present study is the first to offer a bimodal mass spectrometry methodology to assess the impact of *Nosema* on honeybee physiology. Our results clearly suggest that experimental infection with *Nosema* spores impacts the primary targeted gut tissues but also the hemolymph. The latter is the read-out of the bee innate immunity but also and unexpectedly of the bee thoracic muscles. Overall, we found that combining MALDI MFP and MALDI IMS data is a powerful workflow in delivering spatial changes that may occur during stress attacks.

ACKNOWLEDGEMENTS

This work was partially supported by FEAGA (France AgriMer, project HematoBeeTest n° 14-04R). The research leading to these results was also funded by the European Union's Horizon 2020 research and innovation program, under grant agreement No. 773921 (PoshBee). This work was supported by the EDCSV from University of Grenoble Alpes for the PhD allocation of Camille Houdelet. We thank the Association Plateforme BioPark d'Archamps (France) for its technical facilities through its Research & Development program. We would like to thank the Master 1 student François Di Franco, for the dissection and the MALDI MFPs and Nora Touqui for English improvement of the manuscript.

CONFLICT OF INTEREST

The authors declare no conflict of interest.

ASSOCIATED DATA

All the mass spectrometry proteomics data were deposited to the online open access repository Figshare with the following link https://doi.org/10.6084/m9.figshare.17311448.

ORCID

Camille Houdelet https://orcid.org/0000-0002-0836-5202
Karim Arafah https://orcid.org/0000-0002-8153-7568
Michel Bocquet https://orcid.org/0000-0002-1584-1481
Philippe Bulet https://orcid.org/0000-0001-9016-265X

REFERENCES

1. Caprioli, R. M., Farmer, T. B., & Gile, J. (1997). Molecular imaging of biological samples: Localization of peptides and proteins using MALDI-TOF MS. *Analytical Chemistry*, *69*(23), 4751–4760. https://doi.org/10.1021/ac970888i
2. Karlsson, O., & Hanrieder, J. (2017). Imaging mass spectrometry in drug development and toxicology. *Archives of Toxicology*, *91*(6), 2283-2294. https://doi.org/10.1007/s00204-016-1905-6
3. Trim, P. J., & Snel, M. F. (2016). Small molecule MALDI MS imaging: Current technologies and future challenges. *Methods*, *104*, 127-141. https://doi.org/10.1016/j.ymeth.2016.01.011
4. Ly, A., Buck, A., Balluff, B., Sun, N., Gorzolka, K., Feuchtinger, A., Janssen, K.-P., Kuppen, P. J. K., van de Velde, C. J. H., Weirich, G., Erlmeier, F., Langer, R., Aubele, M., Zitzelsberger, H., McDonnell, L., Aichler, M., & Walch, A. (2016). High-mass-resolution MALDI mass spectrometry imaging of metabolites from formalin-fixed paraffin-embedded tissue. *Nature Protocols*, *11*(8), 1428–1443. https://doi.org/10.1038/nprot.2016.081
5. Dueñas, M. E., Essner, J. J., & Lee, Y. J. (2017). 3D MALDI mass spectrometry imaging of a single cell: Spatial mapping of lipids in the embryonic development of zebrafish. *Scientific Reports*, *7*(1), 14946. https://doi.org/10.1038/s41598-017-14949-x
6. Yalcin, E. B., & de la Monte, S. M. (2015). Review of matrix-assisted laser desorption ionization-imaging mass spectrometry for lipid biochemical histopathology. *Journal of Histochemistry & Cytochemistry*, *63*(10), 762–771. https://doi.org/10.1369/0022155415596202
7. Goto-Inoue, N., Hayasaka, T., & Setou, M. (2010). Imaging mass spectrometry of glycolipids. *Methods in enzymology* (Vol. 478, pp. 287–301). Elsevier. https://doi.org/10.1016/S0076-6879(10)78014-9
8. Dilillo, M. (2017). Ultra-high mass resolution MALDI imaging mass spectrometry of proteins and metabolites in a mouse model of glioblastoma. *Scientific Reports*, *7*(1), 603. https://doi.org/10.1038/s41598-017-00703-w.
9. Llombart, V., Trejo, S. A., Bronsoms, S., Morancho, A., Feifei, M., Faura, J., García-Berrocoso, T., Simats, A., Rosell, A., Canals, F., Hernández-Guillamón, M., & Montaner, J. (2017). Profiling and identification of new proteins involved in brain ischemia using MALDI-imaging-mass-spectrometry. *Journal of Proteomics*, *152*, 243–253. https://doi.org/10.1016/j.jprot.2016.11.014
10. Ryan, D. J., Spraggins, J. M., & Caprioli, R. M. (2019). Protein identification strategies in MALDI imaging mass spectrometry: A brief review. *Current Opinion in Chemical Biology*, *48*, 64–72. https://doi.org/10.1016/j.cbpa.2018.10.023

11. Spraggins, J. M., Rizzo, D. G., Moore, J. L., Noto, M. J., Skaar, E. P., & Caprioli, R. M. (2016). Next-generation technologies for spatial proteomics: Integrating ultra-high speed MALDI-TOF and high mass resolution MALDI FTICR imaging mass spectrometry for protein analysis. *Proteomics*, *16*(11-12), 1678–1689. https://doi.org/10.1002/pmic.201600003
12. Amstalden van Hove, E. R., Smith, D. F., & Heeren, R. M. A. (2010). A concise review of mass spectrometry imaging. *Journal of Chromatography A*, *1217*(25), 3946–3954. https://doi.org/10.1016/j.chroma.2010.01.033
13. Chaurand, P., Schwartz, S. A., & Caprioli, R. M. (2002). Imaging mass spectrometry: A new tool to investigate the spatial organization of peptides and proteins in mammalian tissue sections. *Current Opinion in Chemical Biology*, *6*(5), 676–681. https://doi.org/10.1016/S1367-5931(02)00370-8
14. Chaurand, P., Cornett, D. S., Angel, P. M., & Caprioli, R. M. (2011). *From whole-body sections down to cellular level, multiscale imaging of phospholipids by MALDI mass spectrometry*. *10*(2), O110.004259. https://doi.org/10.1074/mcp.O110.004259.
15. Han, C., Li, S., Yue, Q., Li, N., Yang, H., & Zhao, Z. (2019). Polydopamine-capped AgNPs as a novel matrix overcoming the ion suppression of phosphatidylcholine for MALDI MS comprehensive imaging of glycerophospholipids and sphingolipids in impact-induced injured brain. *The Analyst*, *144*(21), 6304–6312. https://doi.org/10.1039/c9an01361j
16. McDonnell, L. A., & Heeren, R. M. A. (2007). Imaging mass spectrometry. *Mass Spectrometry Reviews*, *26*(4), 606–643. https://doi.org/10.1002/mas.20124
17. Stoeckli, M., Chaurand, P., Hallahan, D. E., & Caprioli, R. M. (2001). Imaging mass spectrometry: A new technology for the analysis of protein expression in mammalian tissues. *Nature Medicine*, *7*(4), 493–496. https://doi.org/10.1038/86573
18. Buchberger, A. R., DeLaney, K., Johnson, J., & Li, L. (2017). Mass spectrometry imaging: A review of emerging advancements and future insights. *Analytical Chemistry*, *90*(1), 240–265. https://doi.org/10.1021/acs.analchem.7b04733.
19. Carter, C. L., Jones, J. W., Farese, A. M., MacVittie, T. J., & Kane, M. A. (2016). Inflation-fixation method for lipidomic mapping of lung biopsies by matrix assisted laser desorption/ionization–Mass spectrometry imaging. *Analytical Chemistry*, *88*(9), 4788–4794. https://doi.org/10.1021/acs.analchem.6b00165
20. Bunch, J., Clench, M. R., & Richards, D. S. (2004). Determination of pharmaceutical compounds in skin by imaging matrix-assisted laser desorption/ionisation mass spectrometry. *Rapid Communications in Mass Spectrometry*, *18*(24), 3051–3060. https://doi.org/10.1002/rcm.1725
21. Enthaler, B., Pruns, J. K., Wessel, S., Rapp, C., Fischer, M., & Wittern, K.-P. (2012). Improved sample preparation for MALDI–MSI of endogenous compounds in skin tissue sections and mapping of exogenous active compounds subsequent to ex-vivo skin penetration. *Analytical and Bioanalytical Chemistry*, *402*(3), 1159–1167. https://doi.org/10.1007/s00216-011-5562-6
22. Avery, J. L., McEwen, A., Flinders, B., Francese, S., & Clench, M. R. (2011). Matrix-assisted laser desorption mass spectrometry imaging for the examination of imipramine absorption by Straticell-RHE-EPI/001 an artificial model of the human epidermis. *Xenobiotica*, *41*(8), 735–742. https://doi.org/10.3109/00498254.2011.573015
23. Schulz, S., Becker, M., Groseclose, M. R., Schadt, S., & Hopf, C. (2019). Advanced MALDI mass spectrometry imaging in pharmaceutical research and drug development. *Current Opinion in Biotechnology*, *55*, 51–59. https://doi.org/10.1016/j.copbio.2018.08.003
24. Swales, J. G., Hamm, G., Clench, M. R., & Goodwin, R. J. A. (2018). Mass spectrometry imaging and its application in pharmaceutical research and development: A concise review. *International Journal of Mass Spectrometry*. *90*(10), 6051–6058. https://doi.org/10.1016/j.ijms.2018.02.007
25. Chumbley, C. W., Reyzer, M. L., Allen, J. L., Marriner, G. A., Via, L. E., Barry, C. E., & Caprioli, R. M. (2016). Absolute quantitative MALDI imaging mass spectrometry: A case of Rifampicin in liver tissues. *Analytical Chemistry*, *88*(4), 2392–2398. https://doi.org/10.1021/acs.analchem.5b04409
26. Källback, P., Nilsson, A., Shariatgorji, M., & Andrén, P. E. (2016). MsIQuant – Quantitation software for mass spectrometry imaging enabling fast access, visualization, and analysis of large data sets. *Analytical Chemistry*, *88*(8), 4346–4353. https://doi.org/10.1021/acs.analchem.5b04603
27. Porta, T., Lesur, A., Varesio, E., & Hopfgartner, G. (2015). Quantification in MALDI-MS imaging: What can we learn from MALDI-selected reaction monitoring and what can we expect for imaging? *Analytical and Bioanalytical Chemistry*, *407*(8), 2177–2187. https://doi.org/10.1007/s00216-014-8315-5
28. Rzagalinski, I., & Volmer, D. A. (2017). Quantification of low molecular weight compounds by MALDI imaging mass spectrometry — A tutorial review. *Biochimica Et Biophysica Acta. Proteins and Proteomics*, *1865*(7), 726–739. https://doi.org/10.1016/j.bbapap.2016.12.011
29. Zhou, Q., Fülöp, A., & Hopf, C. (2020). Recent developments of novel matrices and on-tissue chemical derivatization reagents for MALDI-MSI. *Analytical and Bioanalytical Chemistry*. *413*(10), 2599–2617. https://doi.org/10.1007/s00216-020-03023-7
30. Boughton, B. A., & Thinagaran, D. (2018). Mass spectrometry imaging (MSI) for plant metabolomics. In C. António (Éd.), *Plant metabolomics* (Vol. 1778, pp. 241–252). Springer New York. https://doi.org/10.1007/978-1-4939-7819-9_17
31. Dong, Y., Li, B., Malitsky, S., Rogachev, I., Aharoni, A., Kaftan, F., Svatos, A., & Franceschi, P. (2016). Sample preparation for mass spectrometry imaging of plant tissues: A review. *Frontiers in Plant Science*, *7*, 60. https://doi.org/10.3389/fpls.2016.00060
32. Qin, L., Zhang, Y., Liu, Y., He, H., Han, M., Li, Y., Zeng, M., & Wang, X. (2018). Recent advances in matrix-assisted laser desorption/ionisation mass spectrometry imaging (MALDI-MSI) for *in situ* analysis of endogenous molecules in plants. *Phytochemical Analysis*, *29*(4), 351–364. https://doi.org/10.1002/pca.2759
33. Susniak, K., Krysa, M., Gieroba, B., Komaniecka, I., & Sroka-Bartnicka, A. (2020). Recent developments of MALDI MSI application in plant tissues analysis. *Acta Biochimica Polonica*, *67*(3), 277–281. https://doi.org/10.18388/abp.2020_5394
34. Harris, A., Roseborough, A., Mor, R., Yeung, K. K.-C., & Whitehead, S. N. (2020). Ganglioside detection from formalin-fixed human brain tissue utilizing MALDI imaging mass spectrometry. *Journal of the American Society for Mass Spectrometry*, *31*(3), 479–487. https://doi.org/10.1021/jasms.9b00110
35. Seeley, E. H., & Caprioli, R. M. (2011). MALDI imaging mass spectrometry of human tissue: Method challenges and clinical perspectives. *Trends in Biotechnology*, *29*(3), 136–143. https://doi.org/10.1016/j.tibtech.2010.12.002
36. Verhaert, P. D., Conaway, M. C. P., Pekar, T. M., & Miller, K. (2007). Neuropeptide imaging on an LTQ with vMALDI source: The complete 'all-in-one' peptidome analysis. *International Journal of Mass Spectrometry*, *260*(2), 177–184. https://doi.org/10.1016/j.ijms.2006.11.008
37. Nunes, T. M., Mateus, S., Favaris, A. P., Amaral, M. F. Z. J., von Zuben, L. G., Clososki, G. C., Bento, J. M. S., Oldroyd, B. P., Silva, R., Zucchi, R., Silva, D. B., & Lopes, N. P. (2015). Queen signals in a stingless bee: Suppression of worker ovary activation and spatial distribution of active compounds. *Scientific Reports*, *4*(1), 7449. https://doi.org/10.1038/srep07449
38. Pratavieira, M., Menegasso, A. R. da S., Esteves, F. G., Sato, K. U., Malaspina, O., & Palma, M. S. (2018). MALDI imaging analysis of neuropeptides in Africanized Honeybee (*Apis mellifera*) brain: Effect of aggressiveness. *Journal of Proteome Research*, *17*(7), 2358–2369. https://doi.org/10.1021/acs.jproteome.8b00098
39. Pratavieira, M., da Silva Menegasso, A. R., Garcia, A. M. C., dos Santos, D. S., Gomes, P. C., Malaspina, O., & Palma, M. S. (2014). MALDI imaging

analysis of neuropeptides in the Africanized Honeybee (*Apis mellifera*) brain: Effect of ontogeny. *Journal of Proteome Research*, *13*(6), 3054–3064. https://doi.org/10.1021/pr500224b

40. Catae, A. F., Roat, T. C., Oliveira, R. A. D., Nocelli, R. C. F., & Malaspina, O. (2014). Cytotoxic effects of thiamethoxam in the midgut and malpighian tubules of Africanized *Apis mellifera* (Hymenoptera : Apidae). *Microscopy Research and Technique*, *77*(4), 274–281. https://doi.org/10.1002/jemt.22339
41. Catae, A. F., da Silva Menegasso, A. R., Pratavieira, M., Palma, M. S., Malaspina, O., & Roat, T. C. (2018). MALDI-imaging analyses of honeybee brains exposed to a neonicotinoid insecticide: MALDI-imaging of honeybee brains. *Pest Management Science*, *75*(3), 607–615. https://doi.org/10.1002/ps.5226
42. Catae, A. F., Roat, T. C., Pratavieira, M., Silva Menegasso, A. R. D., Palma, M. S., & Malaspina, O. (2018). Exposure to a sublethal concentration of imidacloprid and the side effects on target and nontarget organs of *Apis mellifera* (Hymenoptera, Apidae). *Ecotoxicology*, *27*(2), 109–121. https://doi.org/10.1007/s10646-017-1874-4
43. Pratavieira, M., da Silva Menegasso, A. R., Roat, T., Malaspina, O., & Palma, M. S. (2020). In situ metabolomics of the honeybee brain : The metabolism of l-Arginine through the polyamine pathway in the proboscis extension response (PER). *Journal of Proteome Research*, *19*(2), 832–844. https://doi.org/10.1021/acs.jproteome.9b00653
44. Gallai, N., Salles, J.-M., Settele, J., & Vaissière, B. E. (2009). Economic valuation of the vulnerability of world agriculture confronted with pollinator decline. *Ecological Economics*, *68*(3), 810–821. https://doi.org/10.1016/j.ecolecon.2008.06.014
45. Baylis, K., Lichtenberg, E. M., & Lichtenberg, E. (2021). Economics of pollination. *Annual Review of Resource Economics*, *13*(1), 101420–110406. https://doi.org/10.1146/annurev-resource-101420-110406
46. Kulhanek, K., Steinhauer, N., Rennich, K., Caron, D. M., Sagili, R. R., Pettis, J. S., Ellis, J. D., Wilson, M. E., Wilkes, J. T., Tarpy, D. R., Rose, R., Lee, K., Rangel, J., & vanEngelsdorp, D. (2017). A national survey of managed honey bee 2015–2016 annual colony losses in the USA. *Journal of Apicultural Research*, *56*(4), 328–340. https://doi.org/10.1080/00218839.2017.1344496
47. Potts, S. G., Biesmeijer, J. C., Kremen, C., Neumann, P., Schweiger, O., & Kunin, W. E. (2010). Global pollinator declines: Trends, impacts and drivers. *Trends in Ecology & Evolution*, *25*(6), 345–353. https://doi.org/10.1016/j.tree.2010.01.007
48. Goulson, D., Nicholls, E., Botias, C., & Rotheray, E. L. (2015). Bee declines driven by combined stress from parasites, pesticides, and lack of flowers. *Science*, *347*(6229), 1255957–1255957. https://doi.org/10.1126/science.1255957
49. O'Neal, S. T., Anderson, T. D., & Wu-Smart, J. Y. (2018). Interactions between pesticides and pathogen susceptibility in honey bees. *Current opinion in insect science*, *26*, 57–62.
50. Higes, M., Martín-Hernández, R., Botías, C., Bailón, E. G., González-Porto, A. V., Barrios, L., del Nozal, M. J., Bernal, J. L., Jiménez, J. J., Palencia, P. G., & Meana, A. (2008). How natural infection by *Nosema ceranae* causes honeybee colony collapse: Natural *Nosema ceranae* infection. *Environmental Microbiology*, *10*(10), 2659–2669. https://doi.org/10.1111/j.1462-2920.2008.01687.x
51. Staveley, J. P., Law, S. A., Fairbrother, A., & Menzie, C. A. (2014). A causal analysis of observed declines in managed honey bees (*Apis mellifera*). *Human and Ecological Risk Assessment*, *20*(2), 566–591. https://doi.org/10.1080/10807039.2013.831263
52. Higes, M., Martín, R., & Meana, A. (2006). *Nosema ceranae*, a new microsporidian parasite in honeybees in Europe. *Journal of Invertebrate Pathology*, *92*(2), 93–95. https://doi.org/10.1016/j.jip.2006.02.005
53. Fries, I., Feng, F., da Silva, A., Slemenda, S. B., & Pieniazek, N. J. (1996). *Nosema ceranae* n. Sp. (Microspora, Nosematidae), morphological and molecular characterization of a microsporidian parasite of the Asian honey bee *Apis cerana* (Hymenoptera, Apidae). *European Journal of Protistology*, *32*(3), 356–365. https://doi.org/10.1016/S0932-4739(96)80059-9
54. Martín-Hernández, R., Bartolomé, C., Chejanovsky, N., Le Conte, Y., Dalmon, A., Dussaubat, C., García-Palencia, P., Meana, A., Pinto, M. A., Soroker, V., & Higes, M. (2018). *Nosema ceranae* in *Apis mellifera*: A 12 years postdetection perspective. *Environmental Microbiology*, *20*(4), 1302–1329. https://doi.org/10.1111/1462-2920.14103
55. Badaoui, B., Fougeroux, A., Petit, F., Anselmo, A., Gorni, C., Cucurachi, M., Cersini, A., Granato, A., Cardeti, G., Formato, G., Mutinelli, F., Giuffra, E., Williams, J. L., & Botti, S. (2017). RNA-sequence analysis of gene expression from honeybees (*Apis mellifera*) infected with *Nosema ceranae*. *PloS ONE*, *12*(3), e0173438. https://doi.org/10.1371/journal.pone.0173438
56. Mayack, C., & Naug, D. (2009). Energetic stress in the honeybee *Apis mellifera* from *Nosema ceranae* infection. *Journal of Invertebrate Pathology*, *100*(3), 185–188. https://doi.org/10.1016/j.jip.2008.12.001
57. Mayack, C., Natsopoulou, M. E., & McMahon, D. P. (2015). *Nosema ceranae* alters a highly conserved hormonal stress pathway in honeybees : *Nosema ceranae* alters a hormonal pathway. *Insect Molecular Biology*, *24*(6), 662–670. https://doi.org/10.1111/imb.12190
58. Martín-Hernández, R., Higes, M., Sagastume, S., Juarranz, Á., Dias-Almeida, J., Budge, G. E., Meana, A., & Boonham, N. (2017). Microsporidia infection impacts the host cell's cycle and reduces host cell apoptosis. *PLoS ONE*, *12*(2), e0170183. https://doi.org/10.1371/journal.pone.0170183
59. Antúnez, K., Martín-Hernández, R., Prieto, L., Meana, A., Zunino, P., & Higes, M. (2009). Immune suppression in the honey bee (*Apis mellifera*) following infection by *Nosema ceranae* (Microsporidia). *Environmental Microbiology*, *11*(9), 2284–2290. https://doi.org/10.1111/j.1462-2920.2009.01953.x
60. Li, W., Evans, J. D., Li, J., Su, S., Hamilton, M., & Chen, Y. (2017). Spore load and immune response of honey bees naturally infected by *Nosema ceranae*. *Parasitology Research*, *116*(12), 3265–3274. https://doi.org/10.1007/s00436-017-5630-8
61. Huang, W.-F., Solter, L., Aronstein, K., & Huang, Z. (2015). Infectivity and virulence of *Nosema ceranae* and *Nosema apis* in commercially available North American honey bees. *Journal of Invertebrate Pathology*, *124*, 107–113. https://doi.org/10.1016/j.jip.2014.10.006
62. Roberts, K. E., & Hughes, W. O. (2014). Immunosenescence and resistance to parasite infection in the honey bee, *Apis mellifera*. *Journal of Invertebrate Pathology*, *121*, 1–6. https://doi.org/10.1016/j.jip.2014.06.004
63. Gage, S. L., Kramer, C., Calle, S., Carroll, M., Heien, M., & DeGrandi-Hoffman, G. (2017). *Nosema ceranae* parasitism impacts olfactory learning and memory and neurochemistry in honey bees (*Apis mellifera*). *Journal of Experimental Biology*, *221*(Pt 4), jeb161489. https://doi.org/10.1242/jeb.161489.
64. Goblirsch, M., Huang, Z. Y., & Spivak, M. (2013). Physiological and behavioral changes in honey bees (*Apis mellifera*) induced by *Nosema ceranae* infection. *PLoS ONE*, *8*(3), e58165. https://doi.org/10.1371/journal.pone.0058165
65. Li, H., Zhang, L., Ni, C., Shang, H., Zhuang, S., & Li, J. (2013). Molecular recognition of floral volatile with two olfactory related proteins in the Eastern honeybee (*Apis cerana*). *International Journal of Biological Macromolecules*, *56*, 114–121. https://doi.org/10.1016/j.ijbiomac.2013.01.032
66. Rubanov, A., Russell, K. A., Rothman, J. A., Nieh, J. C., & McFrederick, Q. S. (2019). Intensity of *Nosema ceranae* infection is associated with specific honey bee gut bacteria and weakly associated with gut microbiome structure. *Scientific Reports*, *9*(1), 1–8. https://doi.org/10.1038/s41598-019-40347-6
67. Houdelet, C., Sinpoo, C., Chantaphanwattana, T., Voisin, S. N., Chantawannakul, P., Bulet, P. (s. d.). Proteomics of anatomical sections of the gut of *Nosema*-infected Western honeybee (*Apis mellifera*) reveals different early responses to *Nosema* spp.

isolates. *Journal of Proteome Research*, 2021, *20*(1), 804–817. https://doi.org/10.1021/acs.jproteome.0c00658.
68. Carreck, N. L., Andree, M., Brent, C. S., Cox-Foster, D., Dade, H. A., Ellis, J. D., Hatjina, F., & van Englesdorp, D. (2013). Standard methods for *Apis mellifera* anatomy and dissection. *Journal of Apicultural Research*, *52*(4), 1–40. https://doi.org/10.3896/IBRA.1.52.4.03
69. Arafah, K., Voisin, S. N., Masson, V., Alaux, C., Le Conte, Y., Bocquet, M., & Bulet, P. (2019). MALDI–MS profiling to address honey bee health status under bacterial challenge through computational modeling. *Proteomics*, *19*(23), e1900268. https://doi.org/10.1002/pmic.201900268
70. Croxatto, A., Prod'hom, G., & Greub, G. (2012). Applications of MALDI-TOF mass spectrometry in clinical diagnostic microbiology. *FEMS Microbiology Reviews*, *36*(2), 380–407. https://doi.org/10.1111/j.1574-6976.2011.00298.x
71. Boyer, P. H., Boulanger, N., Nebbak, A., Collin, E., Jaulhac, B., & Almeras, L. (2017). Assessment of MALDI-TOF MS biotyping for *Borrelia burgdorferi* sl detection in *Ixodes ricinus*. *PLoS ONE*, *12*(9), e0185430. https://doi.org/10.1371/journal.pone.0185430
72. Yssouf, A., Almeras, L., Terras, J., Socolovschi, C., Raoult, D., & Parola, P. (2015). Detection of *Rickettsia spp* in ticks by MALDI-TOF MS. *PLOS Neglected Tropical Diseases*, *9*(2), e0003473. https://doi.org/10.1371/journal.pntd.0003473
73. Houdelet, C., Bocquet, M., & Bulet, P. (2020). MALDI Biotyping, an approach for deciphering and assessing the identity of the honeybee pathogen Nosema. *Rapid Communications in Mass Spectrometry: RCM*, *35*(3), e8980. https://doi.org/10.1002/rcm.8980
74. Zhang, Y., Chen, D., Du, M., Ma, L., Li, P., Qin, R., Yang, J., Yin, Z., Wu, X., & Xu, H. (2021). Insights into the degradation and toxicity difference mechanism of neonicotinoid pesticides in honeybees by mass spectrometry imaging. *Science of The Total Environment*, *774*, 145170. https://doi.org/10.1016/j.scitotenv.2021.145170
75. Fujino, Y., Minamizaki, T., Yoshioka, H., Okada, M., & Yoshiko, Y. (2016). Imaging and mapping of mouse bone using MALDI-imaging mass spectrometry. *Bone Reports*, *5*, 280–285. https://doi.org/10.1016/j.bonr.2016.09.004
76. Vandenbosch, M., Nauta, S. P., Svirkova, A., Poeze, M., Heeren, R. M. A., Siegel, T. P., Cuypers, E., & Marchetti-Deschmann, M. (2021). Sample preparation of bone tissue for MALDI-MSI for forensic and (pre)clinical applications. *Analytical and Bioanalytical Chemistry*, *413*(10), 2683–2694. https://doi.org/10.1007/s00216-020-02920-1
77. Li, B., Zhang, Y., Ge, J., Liu, K., & Li, P. (2018). Sample preparation for mass spectrometry imaging of leaf tissues: A case study on analyte delocalization. *Analytical and Bioanalytical Chemistry*, *410*(28), 7449–7456. https://doi.org/10.1007/s00216-018-1355-5
78. Chen, Y., Liu, Y., Allegood, J., Wang, E., Cachón-González, B., Cox, T. M., Merrill, A. H., & Sullards, M. C. (2010). Imaging MALDI mass spectrometry of sphingolipids using an oscillating capillary nebulizer matrix application system. *Mass Spectrometry Imaging* (Vol. 656, pp. 131–146). Humana Press. https://doi.org/10.1007/978-1-60761-746-4_7
79. Yang, E., Gamberi, C., & Chaurand, P. (2019). Mapping the fly Malpighian tubule lipidome by imaging mass spectrometry. *Journal of Mass Spectrometry*, *54*(6), 557–566. https://doi.org/10.1002/jms.4366
80. Schwartz, S. A., Reyzer, M. L., & Caprioli, R. M. (2003). Direct tissue analysis using matrix-assisted laser desorption/ionization mass spectrometry: Practical aspects of sample preparation. *Journal of Mass Spectrometry*, *38*(7), 699–708. https://doi.org/10.1002/jms.505
81. Norris, J. L., & Caprioli, R. M. (2013). Analysis of tissue specimens by matrix-assisted laser desorption/ionization imaging mass spectrometry in biological and clinical research. *Chemical Reviews*, *113*(4), 2309–2342. https://doi.org/10.1021/cr3004295
82. Truong, J. X. M., Spotbeen, X., White, J., Swinnen, J. V., Butler, L. M., Snel, M. F., & Trim, P. J. (2021). Removal of optimal cutting temperature (O.C.T.) compound from embedded tissue for MALDI imaging of lipids. *Analytical and Bioanalytical Chemistry*, *413*(10), 2695–2708. https://doi.org/10.1007/s00216-020-03128-z
83. Lemaire, R., Wisztorski, M., Desmons, A., Tabet, J. C., Day, R., Salzet, M., & Fournier, I. (2006). MALDI-MS direct tissue analysis of proteins: Improving signal sensitivity using organic treatments. *Analytical chemistry*, *78*(20), 7145–7153.
84. Bania, J., Stachowiak, D., & Polanowski, A. (1999). Primary structure and properties of the cathepsin G/chymotrypsin inhibitor from the larval hemolymph of *Apis mellifera*. *European Journal of Biochemistry*, *262*(3), 680–687. https://doi.org/10.1046/j.1432-1327.1999.00406.x
85. Habermann, E. (1972). Bee and wasp venoms. *Science*, *177*(4046), 314–322. https://doi.org/10.1126/science.177.4046.314
86. Neumann, W., Habermann, E., & Amend, G. (1952). Zur papierelektrophoretischen fraktionierung tierischer gifte. *Naturwissenschaften*, *39*(12), 286–287. https://doi.org/10.1007/bf00591257
87. Paris, L., Peghaire, E., Moné, A., Diogon, M., Debroas, D., Delbac, F., & El Alaoui, H. (2020). Honeybee gut microbiota dysbiosis in pesticide/parasite co-exposures is mainly induced by *Nosema ceranae*. *Journal of Invertebrate Pathology*, *172*, 107348. https://doi.org/10.1016/j.jip.2020.107348
88. Dussaubat, C., Brunet, J.-L., Higes, M., Colbourne, J. K., Lopez, J., Choi, J.-H., Martín-Hernández, R., Botías, C., Cousin, M., McDonnell, C., Bonnet, M., Belzunces, L. P., Moritz, R. F. A., Le Conte, Y., & Alaux, C. (2012). Gut pathology and responses to the microsporidium *Nosema ceranae* in the honey bee *Apis mellifera*. *PLoS ONE*, *7*(5), e37017. https://doi.org/10.1371/journal.pone.0037017
89. Kralj, J., & Fuchs, S. (2010). *Nosema sp.* influences flight behavior of infected honey bee (*Apis mellifera*) foragers. *Apidologie*, *41*(1), 21–28. https://doi.org/10.1051/apido/2009046
90. Veillard, F., Troxler, L., & Reichhart, J.-M. (2016). *Drosophila melanogaster* clip-domain serine proteases: Structure, function and regulation. *Biochimie*, *122*, 255–269. https://doi.org/10.1016/j.biochi.2015.10.007
91. Aufauvre, J., Misme-Aucouturier, B., Viguès, B., Texier, C., Delbac, F., & Blot, N. (2014). Transcriptome analyses of the honeybee response to *Nosema* ceranae and insecticides. *PLoS ONE*, *9*(3), e91686. https://doi.org/10.1371/journal.pone.0091686
92. Chaimanee, V., Chantawannakul, P., Chen, Y., Evans, J. D., & Pettis, J. S. (2012). Differential expression of immune genes of adult honey bee (*Apis mellifera*) after inoculated by *Nosema* ceranae. *Journal of Insect Physiology*, *58*(8), 1090–1095. https://doi.org/10.1016/j.jinsphys.2012.04.016
93. Schwarz, R. S., & Evans, J. D. (2013). Single and mixed-species trypanosome and microsporidia infections elicit distinct, ephemeral cellular and humoral immune responses in honey bees. *Developmental & Comparative Immunology*, *40*(3-4), 300–310. https://doi.org/10.1016/j.dci.2013.03.010

SUPPORTING INFORMATION

Additional supporting information may be found online https://doi.org/10.1002/pmic.202100224 in the Supporting Information section at the end of the article.

How to cite this article: Houdelet, C., Arafah, K., Bocquet, M., & Bulet, P. (2022). Molecular histoproteomy by MALDI mass spectrometry imaging to uncover markers of the impact of *Nosema* On *Apis mellifera*. *Proteomics*, *22*, e2100224. https://doi.org/10.1002/pmic.202100224